Computers and Artificial Intelligence; Vol.3, No.6; 2026
E-ISSN: 3006-3728 P-ISSN: 3006-371X
DOI: https://doi.org/10.70267/cai.v3n6.164185
Published by: Zeus Press

Terahertz Integrated Sensing and Communication for Ground-to-UAV Channels: A Survey of Channel Modeling, Waveforms, and Beam Management

Zihan Zhou*

International School, Beijing University of Posts and Telecommunications, Beijing, China

**Corresponding author: Zihan Zhou.*

Abstract

Terahertz (THz) integrated sensing and communication (ISAC) is emerging as a key enabler of sixth generation (6G) networks, and unmanned aerial vehicles (UAVs) are among its most challenging yet valuable host platforms. Over ground-to-UAV links, THz-ISAC payloads promise ultra-high-rate to backhaul and millimeter-level sensing within the stringent size, weight, and power budget of a hovering drone. Realizing this promise requires a coherent understanding of four tightly coupled pillars: the ground-to-UAV THz channel, beam management, the ISAC waveform and its transceiver realization, and system-level performance. This survey is organized around these four pillars. We first consolidate the propagation fundamentals of aerial THz links, including altitude-dependent molecular absorption and UAV-specific non-stationarity, together with the measurement and modeling literature that underpins them. We then review beam management, covering near-field beam-pattern transformation, alignment and tracking under misalignment, and wideband hybrid beamforming that combats beam squint with true-time-delay architectures. We next contrast the candidate ISAC waveforms — OTFS, DFT-s-OTFS with superimposed pilots, and SI-DFT-s-OFDM with flexible guard intervals — in terms of PAPR, power-amplifier efficiency, Doppler robustness, and sensing accuracy, and assess the transceiver hardware against the UAV payload envelope. Finally, we discuss system-level performance, including localization bounds, spectral efficiency, and sensing/vision-aided mobility management, along with use cases and open challenges. Throughout, quantitative claims are traced to their source documents and to the specific figures from which they stem.

Keywords

terahertz, integrated sensing and communication, ground-to-UAV channel, channel modeling, waveform design

1. Introduction

1.1 Background and Motivation

As sixth-generation (6G) research advances toward the ITU's IMT-2030 framework, the demand for ultra-high data rates, ultra-low latency, and ubiquitous connectivity has reached a broad consensus, with Tbps-class throughput and near-zero latency widely set as headline targets [1]. The THz band (0.1–3.0 THz) spans a large, largely unoccupied and, to date, only lightly regulated portion of the radio spectrum and is widely regarded as

© 2026 The Author(s). Authors retain copyright in their articles.

the key spectral resource for Tbps-class transmission and millimeter-level sensing [1, 2]. In parallel, the service boundary of 6G is expanding from terrestrial cellular networks to a multi-dimensional space–air–ground fabric, and ISAC is one of its signature scenarios; this expansion places unprecedented requirements on how precisely the propagation environment must be characterized [3]. The resulting space–air–ground and UAV-ISAC application landscape is illustrated in Fig. 1.

Among aerial platforms, the UAV occupies a unique position: it can be deployed rapidly, hover, and provide line-of-sight-dominated links, yet it imposes severe constraints on payload size, weight, and power. THz-ISAC is attractive here precisely because shared hardware modules allow the communication and sensing payloads to be merged into a single ISAC payload, reducing device size, weight, power consumption, and computational complexity; moreover, the extremely small wavelength at THz frequencies shrinks the transceiver and enables a compact, miniaturized, integrated payload [4].

Figure 1: THz-ISAC in the space–air–ground–sea integrated network. (a) Integrated THz/FSO SAGIN spanning deep-space, GEO and LEO satellites, a space station, HAPS, UAV relay platforms, aircraft backbone networks and ocean-going vessels; (b) representative UAV-ISAC use cases in 6G, including aerial base stations, multi-UAV networks, THz detection, wireless backhaul, ground-to-UAV sensing and communication, augmented/virtual reality, position and localization, and disaster relief

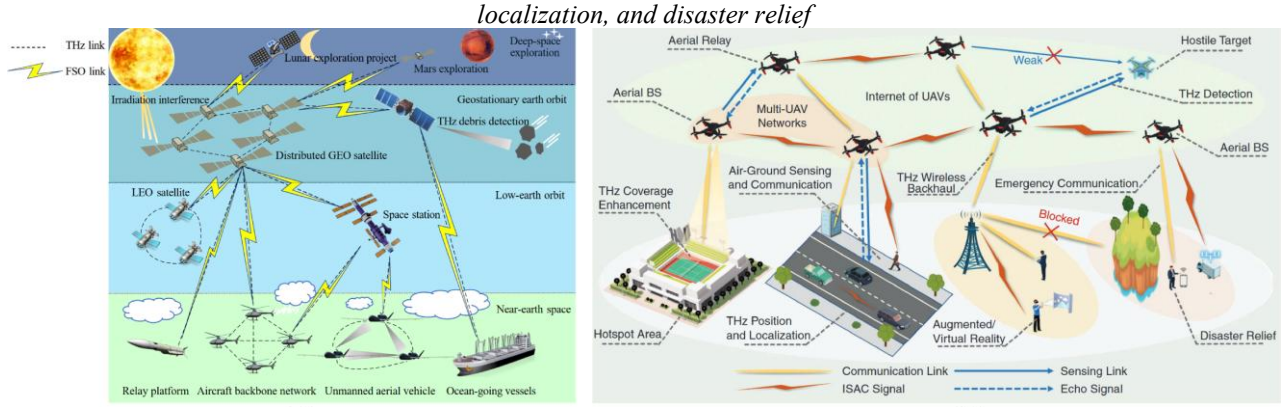

Sources: [4, 5, 6].

1.2 Evolution of THz Channel Research for Aerial Links

Channel models are the fundamental link between physical-layer transmission characteristics and system-level performance evaluation. Early THz channel studies borrowed the mature methodology of the microwave and millimeter-wave (mmWave) bands [7]; however, the strong molecular absorption, rough-surface scattering, and extreme line-of-sight (LoS) dependence of THz waves mean that the conventional framework may face significant challenges at THz frequencies [1]. As measurement instruments such as vector network analyzers (VNAs), sliding correlators, and THz time-domain spectroscopy (THz-TDS) matured, research shifted from large-scale path-loss characterization toward fine-grained joint delay–angle and cluster-level modeling, and channel models evolved from deterministic ray tracing toward statistical and hybrid models [1, Sec. II], [2, Sec. IV].

For aerial links, this evolution is still at an early stage: the first dedicated ground-to-UAV sub-THz measurement campaign at 140 GHz was reported only recently [8], and airborne THz measurements have begun to reveal altitude dependence that has no terrestrial counterpart [6].

1.3 Current Research Hotspots

Research is advancing along two fronts. First, extensive measurement and modeling work has been carried out in terrestrial scenarios (indoor offices, urban microcells (UMi), data centers, and device-to-device (D2D) environments) [5, 9, 10, 11]. Second, aerial and non-terrestrial scenarios, UAV relays, low-Earth-orbit inter-satellite links, and maritime communication, are rapidly becoming a new research frontier [6, 8, 12, 13]. What makes this trend distinctive is the introduction of ISAC: channel models must now serve not only demodulation and equalization but also target detection, ranging, and velocimetry. This has given rise to the emerging cross-

© 2026 The Author(s). Authors retain copyright in their articles.

disciplinary topic of joint communication–sensing channel characterization, and has drawn attention to waveform design, channel estimation, and joint acquisition of sensing parameters [4, 14, 15, 16].

1.4 Key Gaps

Despite intense activity, several gaps remain. **(i) Unified cross-domain modeling for ground-to-UAV links.** Most measurements focus on a single scenario; because the channel characteristics differ greatly between the ground and air domains, no unified cross-domain channel model has yet emerged, which constrains cross-layer co-design of integrated ground-to-UAV networks [17, 18, 2, Sec. IV]. **(ii) ISAC-driven joint characterization.** Mainstream models target pure communication and lack theoretical support for the multi-dimensional joint parameter representation (e.g., joint delay–Doppler–angle spectra, radar-cross-section mapping) required by ISAC [4, 16]. **(iii) Data scarcity above 300 GHz and real-time tracking.** Existing measurements concentrate on the sub-THz bands around 140/220/300 GHz, while data above 300 GHz remain scarce, and real-time channel tracking and prediction in highly dynamic scenarios are still in their infancy [6, 9, 16, 19]. **(iv) Waveform–beam co-design under UAV dynamics.** The combination of severe Doppler, PAPR-constrained power amplifiers, and a rapidly increasing beam-search overhead is only partially addressed [4, 20, 21, 22, 23, 24].

1.5 Contributions and Organization

This survey makes the following contributions. (1) It consolidates the propagation fundamentals of THz ground-to-UAV links, explicitly separating distance-dependent loss from altitude-dependent molecular absorption and thereby isolating the UAV-specific propagation peculiarities that terrestrial surveys leave unaddressed [1, 16]. (2) It re-organizes the measurement methodology and modeling literature around the UAV context and highlights the ground-to-UAV geometry-based stochastic model. (3) It presents, side by side, the waveform options for THz-ISAC and their quantified trade-offs. (4) It reviews beam management and hardware enablers against the UAV payload envelope and traces, where feasible, every quantitative claim to its source and to the relevant figure. The remainder of the paper follows the four-pillar structure: Section 2 consolidates channel modeling (propagation fundamentals, measurement, and modeling), Section 3 covers beam management, Section 4 covers waveform design together with its transceiver implementation, and Sections 5 and 6 discuss system-level performance, open challenges, and conclusions. Fig. 2 illustrates this four-pillar organization.

Figure 2: Organization of this survey around four coupled pillars: THz channel modeling for ground-to-UAV links; beam management and beamforming; waveform design and transceiver implementation; and system-level performance and applications

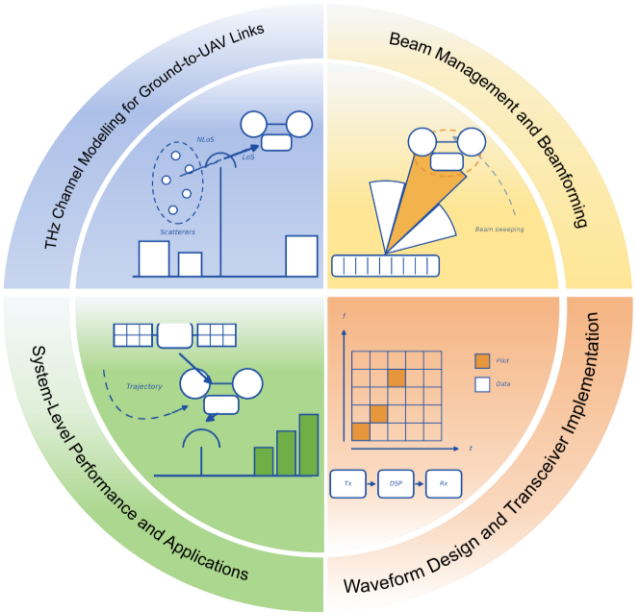

© 2026 The Author(s). Authors retain copyright in their articles.

2. THz Channel Modeling for Ground-to-UAV Links

This section develops the channel pillar along the natural chain from physics to data to models. We first consolidate the propagation fundamentals that set the physics of the ground-to-UAV THz link (Section 2.1); we then review how such links are sounded and how multipath parameters are extracted from measurement campaigns (Section 2.2); and we finally distill these results into statistical, deterministic and geometry-based models, singling out the first dedicated ground-to-UAV GBSM (Section 2.3).

2.1 Propagation Fundamentals

2.1.1 Spectrum Resources, Standardization, and Research Landscape

The first wireless-communication standard at 300 GHz was defined by the IEEE 802.15 THz Interest Group as IEEE 802.15.3d-2017, an amendment to the 60 GHz IEEE 802.15.3-2016 standard, for operation up to 100 Gbps [2, 25]. The 300 GHz system can utilize 8 different channel bandwidths between 252 and 321 GHz at multiples of 2.16 GHz; both single-carrier and on-off modulation schemes are combined with LDPC and Reed–Solomon codes, and the identified applications include point-to-point kiosk download, data-center communication, fronthaul/backhaul, intra-device communication, and WLANs [1]. The same source stresses that profound knowledge of the propagation channel is crucial, yet channel modeling at THz frequencies is still in its infancy, having been mostly limited to fixed point-to-point scenarios up to 300 GHz [1]. Importantly, the THz band is not expected to replace the sub-6 GHz and mmWave bands but to complement them within a heterogeneous spectrum architecture, owing to the severe propagation and hardware challenges that still span the so-called terahertz gap [15].

2.1.2 Free-Space Path Loss, Antenna Aperture Effect, and Absorption Windows

Free-space path loss (FSPL) is the inevitable attenuation experienced by a wave between two isotropic antennas [1, Eq. 9]. Over 1–3000 GHz, substantial loss already exceeding 100 dB appears at 100 GHz, with a 20 dB-per-decade increase, i.e., a further ~20 dB from 0.1 to 1 THz and ~10 dB from 1 to 3 THz [1]. Crucially, if the antenna aperture ratios A_{et}/λ and A_{er}/λ are maintained across frequency, the received power decreases with the square of both frequency and distance, while the path loss itself is unchanged, so the required antenna size shrinks at higher frequencies; however, the aperture efficiency of horns and dishes falls consistently, array feed losses grow with element count, and physical feed spacing becomes impractical, so an unbounded aperture increase is inhibited [1].

Beyond spreading, molecular absorption dominates: when the THz wavelength becomes comparable to the rotational and vibrational scales of water-vapour and oxygen molecules, resonances produce large attenuation peaks [1]. Oxygen contributes insignificantly above 300 GHz and absorption is water-vapour-dominated; below 300 GHz attenuation is minimal (up to a few dB), whereas in the spectral windows W1 = [331–375 GHz], W2 = [385–440 GHz], W3 = [453–510 GHz], W4 = [630–705 GHz], and W5 = [815–890 GHz] attenuation reaches up to 100 dB/km [1]. Computation relies on HITRAN spectroscopic data with radiative-transfer theory, the Van Vleck–Weisskopf line shape, the Beer–Lambert law, or the ITU-R P.676 model for 10–1000 GHz [1, 7].

2.1.3 Meteorological Attenuation: Rain, Snow, Fog, and Cloud

Additional outdoor attenuation arises from rain and snow. Rain attenuation $\gamma_R = kR^a$ (dB/km) follows the ITU model, with polarization-dependent coefficients because droplet shape and size are comparable to the wavelength; the loss versus rain rate (from <1 mm/h light rain to >50 mm/h extreme rain) flattens around 100 GHz, beyond which no additional attenuation is expected within the bands of interest up to 3 THz [1]. The physical reason is the transition from Rayleigh to Mie scattering. Snow has no equivalent ITU model and is treated as rain [1]. Fog and cloud are treated as the same phenomenon differing only by height above ground, with specific attenuation $\gamma_c = K_l(f, T)\cdot M$, where M is liquid-water density [1, Eq. 11]. For medium fog/cloud (visibility ~300 m) and heavy fog/cloud (visibility ~50 m), the attenuation at 100 GHz is about 5 dB/km with a ~15 dB increase from 0.1 to 1 THz for the worst case; unlike FSPL and atmospheric absorption, these losses are comparatively small and can be readily compensated [1]. Nevertheless, they must be accounted for in accurate channel characterization and, for outdoor and ground-to-UAV links, they bound availability.

© 2026 The Author(s). Authors retain copyright in their articles.

2.1.4 Measured Path Loss, Shadowing, Blockage, and NLoS Excess Loss

Measured large-scale behavior validates, with instructive deviations, the theoretical framework. In an indoor hall at 99–101 GHz, the fitted path loss PL = 1.77·10·log₁₀(d) + 74.40 dB achieves $R^2 = 0.95$, and the path-loss exponent α = 1.77 is smaller than the theoretical FSPL value of 2, primarily because of waveguiding effects; shadowing follows N(0, 1.85) [10]. In urban outdoor D2D at 145–146 GHz, LoS observations closely follow FSPL, with path-loss coefficients between 1.77 and 1.84 (below the FSPL coefficient of 2; this is physically reasonable because the received signal contains reflected multipath components in addition to the d^{-2} LoS term), and the shadowing standard deviation is only 1.63 dB; the commonly used log-normal model provides an excellent fit [11]. For NLoS, an offset of 10–15 dB relative to FSPL is observed, with slopes around 1.5 (OLS) or 2 (weighted regression), and shadowing standard deviations σ_omni = 5.37 and σ_max-dir = 7.53 dB, at least four times larger than their LoS counterparts [11]. Importantly, the extracted parameters are valid only over the measured range (1–100 m) [11]. Human blockage is likewise dynamic and MAC-relevant: a simple shadowing-event model parameterized by duration t_D, decay time t_decay, rise time t_rise, and mean attenuation A_mean is available, and diffraction can be modeled by two knife edges around the body [26]. Fig. 3 contrasts the fitted exponents and shadowing of best-directional and omnidirectional processing against the 3GPP LoS/NLoS models and FSPL.

Figure 3: Measured path loss and frequency-dependent atmospheric attenuation for sub-THz ground links. (a) LoS and (b) NLoS path loss versus distance in the indoor-office scenario; (c) LoS and (d) NLoS path loss in the urban-microcell (UMi) scenario, all compared with the 3GPP LoS/NLoS models and FSPL; (e) gaseous absorption of dry and standard air up to 1 THz, showing the water-vapor absorption lines and the 17.1 dB/m peak near 557 GHz.

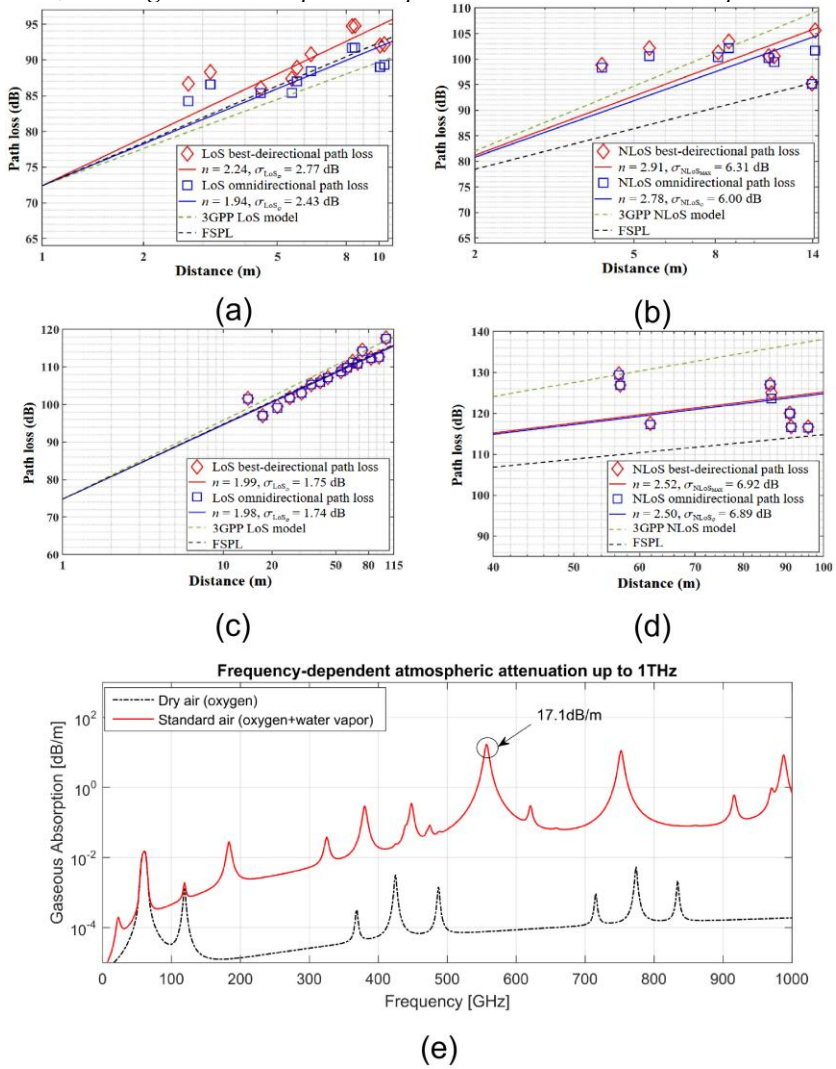

Sources: [1, 9].

© 2026 The Author(s). Authors retain copyright in their articles.

2.1.5 UAV-Specific Propagation Peculiarities

Three effects distinguish the ground-to-UAV channel from its terrestrial counterpart.

Altitude-dependent molecular absorption. Because molecular-absorption loss increases with both temperature and pressure, it decreases rapidly with altitude (lower pressure, colder air), becoming almost negligible above 10 km [27]. This makes the effect not only distance- but also altitude-dependent, and yields a counter-intuitive trade-off: for selected THz subbands, starting from a given altitude a notably longer (e.g., 200 km) airplane-to-LEO-satellite link features *lower* loss than a comparable airplane-to-ground link no more than 10 km away [6].

Non-stationary, Doppler-heavy channels. Unlike the conventional terrestrial environment, where the channel is time-stationary, high-mobility UAV platforms at THz carrier frequencies introduce more severe Doppler than at mmWave, significantly reducing the channel coherence time; in addition, wind effects cause extra random movement and rotation of the UAV, generating additional Doppler shifts and further constraining the coherence time [4, 17].

Near-field and beam-split behavior. To compensate for substantial THz attenuation, ultra-massive (UM) antenna arrays are employed to form pencil beams with ultra-high array gain; because of the ultrawide bandwidth, the generated narrow beams disperse and split into surrounding directions at different frequencies, i.e., the beam-split effect [4]. Moreover, the spherical-wave (near-field) model must be used when the distance is shorter than the Rayleigh distance, which grows with the square of the array aperture: for a 0.1 m aperture this distance is 4 m at 60 GHz but approximately 40 m at 0.6 THz [16, 28]. Quantitatively, the beam split is approximately 4° (1.4°) at 0.3 THz for 30 GHz (2 GHz) bandwidth for a broadside target direction-of-arrival [16], and the THz path loss reaches ≈120 dB/100 m at 0.6 THz [16].

2.2 Channel Measurement Methodology and Campaigns

Fundamentals alone do not produce models, they must be anchored in measurement. We therefore turn to the sounding methodology and to the campaigns that have generated the still-sparse ground-to-UAV evidence base.

2.2.1 Sounding Techniques and System Architectures

Three families of sounding techniques dominate THz channel measurement. THz time-domain spectroscopy (TDS) probes material and channel properties with ultra-short light pulses converted to the THz range by photo-conductive switches; the received complex signal yields the complex refractive index and supports time-gating for SNR enhancement, offering bandwidths up to 10 THz, dynamic range around 100 dB, and femtosecond timing resolution [1]. THz frequency-domain spectroscopy (FDS) uses continuous-wave radiation and optical heterodyne detection, providing roughly 100 dB dynamic range over about 6 THz at 10 MHz frequency resolution and lower cost; like TDS, however, its low output power and large footprint prevent long-range characterization, and it cannot capture Doppler because the channel must remain stationary for the whole measurement [1]. Vector-network-analyzer (VNA) setups connect a VNA to frequency extenders and horn antennas and require lengthy SOLT calibration; because the extenders must be cabled and phase-synchronized, the Tx–Rx separation is constrained, the VNA body acts as an unwanted reflector, and the long sweep time exceeds the coherence time of time-variant channels, precluding Doppler capture — yet the VNA provides about 120 dB dynamic range and very high delay resolution, resolving a large number of multipath components (MPCs) [1]. Correlation-based (sliding-correlator) sounders mix a pseudo-noise sequence up to the target band and recover the complex channel impulse response with Tx/Rx clock synchronization, so they can measure a dynamic channel but not a mobile one [1]. Recent surveys compare these architectures, including frequency-domain VNA systems with up-conversion modules, a 260–400 GHz VNA system, and time-domain correlation and TDS platforms [3]; VNA-based systems are inherently synchronized and of low complexity, but frequency sweeping is time-consuming and the basic setup requires transmission lines between the transceivers, which radio-over-fibre extension can remove to enable long-distance outdoor measurements [3]. A representative THz sounding platform radiates an ASK-modulated 511-sample PN9 sequence of 0.85 μs duration through a high-gain horn antenna, with a symmetrical down-conversion chain at the receiver [9].

© 2026 The Author(s). Authors retain copyright in their articles.

2.2.2 Measurement Campaigns, Scenarios, and Transceiver Geometry

A representative set of campaigns spans the relevant scenarios. **At 100 GHz indoor office** (17.51 × 6.78 m²), LoS receiver locations at 4.5–10.4 m and NLoS locations at 4.2–14.2 m are measured with azimuthal rotation in 20° steps (one HPBW) and elevation tilts of ±15° [9]. **At 132 GHz in an urban-microcell (UMi) scenario**, Tx/Rx heights of 11.6 m and 1.5 m are held throughout, with LoS distances of 14.2–102.7 m and NLoS distances of 56.7–76.4 m, using 10° azimuth steps and ±9° elevation tilts, and 50 IQ snapshots per angle combination [9]. **At 145–146 GHz urban D2D**, 38 locations and nearly 50,000 impulse responses cover LoS and NLoS over 1–100 m at both link ends at the same height, including the "Epstein Family Plaza/VHE" quadrangle and the "Childs and Watt Way" intersection [11]. **At 99–101 GHz indoor hall**, 55 Tx–Rx deployment locations in a 62.2 × 39 m² hall plus a 33 × 2.9 m² corridor, with Tx–Rx distances of 3–58 m, form two L-shaped routes (Route 1 and Route 2) realized by a virtual uniform circular array of radius 6.7 cm and 1° rotation, yielding 55 × 360 = 19,800 channel frequency responses; the transmitter was placed near a wall to mimic a base station, and both ends were 1.3 m high [10]. Table 1 of [5] consolidates ground-scenario measurements for indoor office, wireless data center, kiosk, and smart rail [4, Tbl. 1], [19].

The ground-to-UAV case, though sparse, is decisive for this survey. At 140 GHz, the transmitting antenna is set at an elevation angle of 8° and the receiving antenna at −8° so that the main lobe stays pointing at the receiver throughout the flight path; the half-power beamwidth (HPBW) of the antenna with a 10 cm lens is approximately 5.7°, measured over a 52 cm distance, emphasizing the need for precise alignment [8, 29]. Across three UAV flights, the maximum detected SNR is 10.28 dB, slightly below the static-station value (~11.1 dB) and within ~0.8 dB of the Friis prediction (11.07 dB), indicating near-perfect alignment and a BER below 10^{-10} with ASK modulation; UAV hovering instability introduces variability, and the noise level increases at take-off, plausibly due to rotor-blade modulation [8]. For airborne links, molecular absorption becomes altitude-dependent as described in Section 2.1.5 [6].

2.2.3 Channel Parameter Estimation and MPC Trajectory Tracking

Parameter extraction from directional measurements is a prerequisite for MPC-level modeling. A beamforming-based algorithm (FIBF) applied to a uniform circular array achieves approximately invariant beam patterns over broad bands and constant patterns over the UCA plane, and supports wideband joint delay-and-angle-of-arrival estimation in both near-field and far-field cases; because FIBF can produce pronounced sidelobes that are erroneously identified as paths, successive interference cancellation (SIC) is incorporated, yielding a generic algorithm applicable to far/near-field, wideband/narrowband, and omni/directive arrays [10]. Applied to Rx 15, the method detects eight paths using a 30 dB dynamic range [10]. MPC trajectory tracking then links the estimated components geometrically: for Routes 1 and 2 the total numbers of detected MPC trajectories are 30 and 26, respectively, with dominant trajectories identified by power level; Trajectory 1 is the LoS, Trajectory 2 is the reflection from the back wall behind the transmitter, and Trajectories 3–5 are reflections from metal pillars (Trajectory 5 is received at only 3 Rx locations because of front-pillar blockage); for Route 2 the AoAs of the trajectories concentrate in the regions facing the transmitter ([−100, −80] °) and facing away ([80, 120] °). Comparing propagation delay and AoA with the hall geometry shows that the MPC trajectories match the geometry well [10, 30].

2.3 Channel Characterization and Modeling

With the sounders and the measured datasets above in place, this subsection distils the characterization results into models, moving from empirical delay and angular statistics to deterministic, statistical and geometry-based formulations.

2.3.1 Power-Delay Profiles, Delay Spread, and Angular Statistics

Representative power-delay profiles (PDPs) reveal the multipath structure. In the LoS case at d = 98.4 m, besides a strong peak at the LoS distance, multiple MPCs arise from interaction with environmental objects; the multipath structure is much more pronounced in the omnidirectional than in the directional case, because reflected paths depart and arrive over a wide angular range, the furthest components ($d \geq 200$ m) are more than 40 dB below the strongest, and closer components may be only 20 dB lower; directional processing filters out the extra components through the horn antennas at both ends [11]. NLoS scenarios are generally richer in MPCs because the dominant LoS component is missing; street-canyon NLoS (e.g., at the "Childs and Watt

© 2026 The Author(s). Authors retain copyright in their articles.

Way" intersection) can be remarkably LoS-like, with some very strong components due to strong building-wall reflections and few propagation directions, whereas vegetation-rich quadrangles show many components of similar power [11]. Omnidirectional delay spreads up to 100 ns and directional delay spreads up to 10 ns are observed, with a surprisingly large number of MPCs for 1 GHz bandwidth and 13° beamwidth [11, 30]. In the directional case the delay spread decreases with distance and the confidence interval contains only negative values with a larger absolute slope than in LoS; in the omnidirectional case it also decreases with distance, but less pronouncedly [6, Sec. IV]. Angular spread is considerably lower for LoS than for NLoS; as distance increases, the LoS angular spread increases — the power difference between the LoS component and the rest shrinks — while the NLoS angular spread decreases [11]. Angular power spectra (APS) confirm this: the LoS APS concentrates power in the LoS direction, with smaller contributions about 20 dB below from the back of the transmitter and receiver (attributable to a banner behind the transmitter, not to antenna back lobes, which are about 30 dB down), while street-canyon NLoS shows peaked APSs and the courtyard shows larger dispersion with more than one MPC cluster [11]. Fig. 4 consolidates these statistics from the indoor-hall measurement campaign.

Figure 4: Channel statistics from sub-THz indoor-hall measurements. (a) Delay spread versus distance for the two routes and four receiver groups; (b) empirical CDF of the delay spread with a log-normal fit N(1.26, 0.07); (c) power-delay profile exhibiting a long-delay multipath component; (d) K-factor versus distance; (e) empirical CDF of the K-factor with a normal fit N(6.36, 10.12); (f) power-delay profile for a second receiver pair

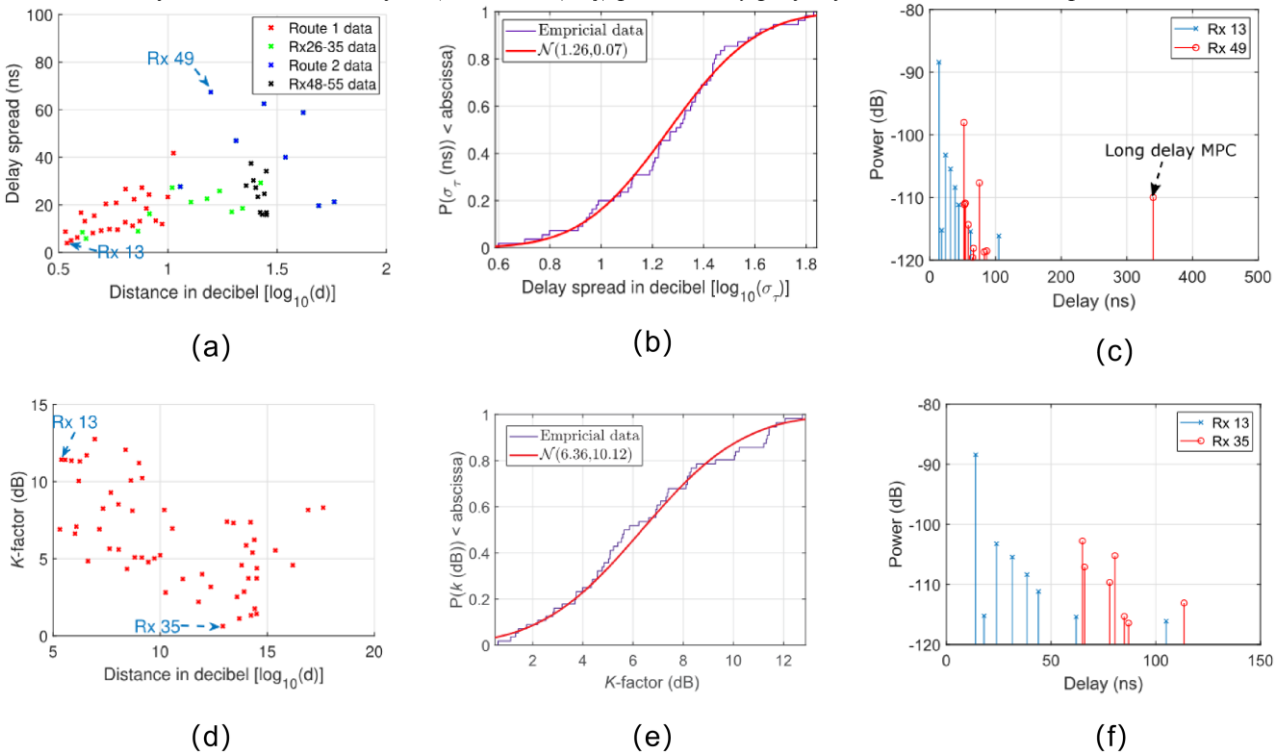

Source: [10].

2.3.2 Statistical Modeling

The composite channel parameters, path loss, delay spread, angular spread, and K-factor, are computed from the extracted MPC parameters, and it is found that the delay and angular spreads statistically obey log-normal distributions while the K-factor obeys a normal distribution, with the fitting parameters concluded for statistical modeling [10]. The path-loss and shadowing models described in Section 2.1.4 [10, 11] provide the large-scale counterpart. Together these constitute the empirical basis for scenario-specific statistical models.

2.3.3 Deterministic, Geometry-Based, and Standardized Models

Modeling approaches range from deterministic to statistical [7]. Ray tracing provides site-specific determinism; the Bello function formalism describes wide-sense-stationary uncorrelated-scattering behavior; the Saleh–Valenzuela (S–V) model captures clustered multipath; and cluster geometry-based stochastic

© 2026 The Author(s). Authors retain copyright in their articles.

models (GBSM) reproduce spatial statistics. A 3GPP-like GBSM has been formulated and validated against experimental observations, thereby bridging the gap between measurements and standards [9]. Directional-path-loss and breakpoint-distance effects also scale with frequency: the breakpoint distance, at which the slope of the path-loss-versus-distance plot changes, increases linearly with frequency in situations with a LoS and a ground-bounce component [9, Sec. III-A].

2.3.4 Ground-to-UAV GBSM and Modeling Gaps

For the aerial case, a three-dimensional GBSM has been introduced that accounts for the complexity of 3D UAV movement and orientation and incorporates the antenna radiation pattern, with special attention to the beam-alignment area during flight, i.e., the region within which the power reduction remains below 3 dB. Its analysis reveals a notable discrepancy between the beam-alignment-area diameter (42 cm) and the HPBW (46 cm) at the UAV side, underscoring the tangible impact of UAV movement on antenna orientation and location. The model uses the closed-form link budget $SNR(dB) = P_T + G_Tx + G_Rx - 10\alpha \cdot \log_{10}(d) - \eta - N - \xi$, combining the path-loss exponent and small-scale fading in the hovering state [7, Sec. III]. This is a first step; dedicated air-ground statistical models remain scarce, and the extension of terrestrial GBSMs to altitude-dependent absorption and non-stationary, wind-driven geometry is an open problem [17, 18]; the general 3D space–time–frequency non-stationary THz GBSM of Wang et al. [31] offers a transferable foundation that can be specialized to such UAV-specific geometry (Section 2.1.5, Section 6.1).

3. Beam Management and Beamforming

3.1 Beamforming Gain, Beam Patterns, and Coverage Extension

Because spreading loss increases with the square of frequency, THz systems must use larger arrays with higher beamforming gains to achieve the same range as mmWave [32]. Increasing the array aperture, however, brings two problems: the number of candidate beams rises sharply, and the Rayleigh distance $2D^2/\lambda$ grows — for an aperture of 0.087 m it is about 1.5 m at 30 GHz but around 22 m at 220 GHz, exceeding the expected coverage of most 6G indoor hotspots [14]. This produces a new near-field regime in which the 3 dB beam pattern changes from an angle-dependent beam into a distance–angle-dependent ellipse [14, 28]. The resulting transition of the Rayleigh distance — from a few meters at mmWave to tens of meters at THz for the same aperture — is a defining signature of THz beam management that has no equivalent in 5G mmWave systems [14, 16]. Coverage can also be understood through array scaling: when the number of elements scales linearly with frequency (constant antenna area), the coverage distance becomes frequency-independent, because the antenna-gain increase fully compensates the isotropic path-loss increase, although practical limits arise from the number of power amplifiers and RF components [26]. At 100 m, the path loss at 100 GHz is approximately 30 dB greater than at 2 GHz, which reduces the feasible inter-site distance and must be counteracted by higher array gain [9, Sec. III-A]. For ground-to-UAV links specifically, the 3 dB range — the beamwidth boundary within which channel-power attenuation is limited to 3 dB despite UAV motion — is linearly correlated with the HPBW over distances from 10 m to 200 m; as the HPBW widens, the required alignment precision diminishes, which fundamentally enhances the resilience of the ground-to-UAV channel to minor positional or angular discrepancies [8].

3.2 Beam Alignment, Tracking, and Misalignment Suppression

Beam alignment techniques fall into two categories: beam training, which transmits known signals and adjusts beamforming parameters, and beam estimation, which estimates channel state information (CSI) and refines the beamforming parameters accordingly [15, 32]. For highly mobile UAV networks, a high–low-frequency cooperative framework is attractive: after locating the communication nodes, the UAV performs beam training using a predefined hierarchical codebook until a suitable beam pair is found; once a reliable THz link is established, it records the beam pair and monitors signal quality, and when the decoder SNR falls below a threshold it initiates beam tracking whose mode depends on the number of recorded beam pairs (three or more, or otherwise) [20, 33, 34]. In a 0.3 THz scenario with 30 dB antenna gain and 25 dBm transmit power, a threshold-based tracking strategy with an $N = 64$ codebook maintains a beam gain indistinguishable from the $N = 32$ case while keeping the beam-search count low; without the threshold, the $N = 64$ setup incurs frequent, unnecessary searches and much higher overhead, and a UAV that does not track at all suffers severe

© 2026 The Author(s). Authors retain copyright in their articles.

attenuation once the initial beam pair degrades [20]. ISAC offers a further step change: an ISAC-assisted scheme uses reference or data signals to perceive the surroundings and anticipate user trajectories, so that base stations can initiate beam reselection before potential blockages occur. This predict-and-prevent procedure reduces the beam-misalignment probability by about 70% compared with networks without sensing; whereas narrower beams without sensing cause the misalignment probability to grow rapidly, the ISAC-aided scheme shows only a slight increment, allowing THz networks to use narrower beams for coverage while maintaining reliable connections [14, 23, 35]. The scheme is best suited to highly mobile but less dense (e.g., highway) scenarios [14, 36].

3.3 Wideband Hybrid Beamforming: Beam Squint, TTD/FTTD, and Array Architectures

Hybrid beamforming combines analog and digital processing and substantially reduces the number of RF chains required relative to fully digital UM-MIMO, which would need a dedicated RF chain per element and is prohibitively complex for UAV platforms [4]. Its central difficulty at THz is beam squint: phase shifters (PSs) can only generate frequency-independent weights, so the beam points in different directions at different subcarrier frequencies [37]. In a 1024-antenna system with f_c = 300 GHz and B = 50 GHz, the array-gain loss caused by beam squint reaches 22 dB at 275 GHz, and narrowband beamforming achieves an average array gain of only 9.4 dB, more than 20 dB below the maximal 30.1 dB [38]. True-time-delay (TTD) elements generate frequency-proportional phases and solve this problem, but a fully-connected TTD (FC-TTD) architecture is power- and complexity-hungry: an adjustable TTD consumes about 80 mW with 10 dB insertion loss, and each THz time delayer consumes about 100 mW versus 40 mW for a PS [16, 38]. A TTD-aided architecture inserts a limited number of adjustable TTDs but still relies on power-hungry tunable delays. The DS-FTTD architecture instead uses low-cost fixed TTDs (realized by a fixed-length microstrip line or waveguide) together with a switch network that enables dynamic FTTD-to-antenna connections; the average array gain rises from 13.3 dB (Q = 4) to 29.1 dB (Q = 128), and for $Q \geq 64$ the loss relative to the maximal array gain is about 1 dB [38]. Owing to its lower hardware complexity and insertion loss, DS-FTTD achieves higher energy efficiency than GoSA, DS-PS, and AoSA-PS — by 55.2%, 75.5%, and 114.2% respectively at 1024 antennas — while its spectral efficiency is only 3.6 and 2.9 bit/s/Hz below FC-TTD and TTD-aided, an acceptable trade-off for UM-MIMO [38]. It also retains over 80% of the perfect-CSI spectral efficiency even with $\xi = 0.6$, and the RD algorithm converges in about eight iterations [38]. On the array side, FCA needs KM PSs whereas AoSA and GoSA employ QN and N PSs respectively, reducing consumption by approximately 80× and 200× compared with FCA, although the sub-arrayed connection yields lower spectral efficiency and localization performance because of fewer degrees of freedom [16]. Near-field ISAC beamforming performs close to fully digital ISAC and communications-only beamformers (with trade-off parameters 0.5 and 1, respectively), and imposing a far-field assumption while designing the OMP dictionary degrades spectral efficiency markedly [16, 28].

3.4 CSI Acquisition and Training

Acquiring CSI for ISAC is daunting at THz: the high-dimensional communication and sensing channels resulting from the large bandwidth and antenna count impose significant challenges, and the extremely narrow UM-MIMO beam sharply increases the number of required beams, incurring considerable search overhead for target search. A unified tensor framework has been proposed that improves estimation accuracy, sensing resolution, and overhead reduction simultaneously [4, 39, 40].

4. Waveform Design and Transceiver Implementation

This section covers the waveform pillar together with the transceiver that realizes it. It first reviews the waveform requirements and the candidate THz-ISAC families with their quantified trade-offs (Section 4.1), and then examines how those waveforms are implemented in the UAV payload, RF front end, antennas and digital back-end (Section 4.2).

© 2026 The Author(s). Authors retain copyright in their articles.

4.1 Waveform Design

Waveform design determines how the single THz-ISAC signal is shaped to serve communication and sensing at once. We begin with the requirements, survey the candidate families, and close with a quantified comparison.

4.1.1 Waveform Requirements: PAPR/PA Efficiency, Doppler, and Phase Noise

Waveform design is a first-order concern at THz, because both communication performance and sensing accuracy are affected by Doppler and peak-to-average-power (PAPR) impairments that are far more severe than at microwave frequencies [21]. Two challenges dominate. First, towards higher carrier frequencies the Doppler-spread effect becomes more severe, especially in high-mobility scenarios: fast time-varying channels with high Doppler spread cause inter-carrier interference (ICI) in the time–frequency domain, and waveforms operating in that domain, such as OFDM and DFT-spread OFDM (DFT-s-OFDM, i.e., SC-FDMA), struggle to equalize the multiple Doppler shifts along each path [17, Sec. I], [24]. Second, as the operating frequency rises, the saturated output power of PAs decreases rapidly despite advances in integrated-circuit technology, so the PAPR requirement on the transmit signal becomes even stricter than in the microwave band [17, Sec. I-A], [18, Sec. I-A]. For UAV platforms, communication and sensing are assessed by different metrics, so designing THz-ISAC waveforms that satisfy both is critical; PAPR additionally forces power back-off in the THz RF front end and thereby limits the communication and sensing ranges [4]. Phase noise is a further THz-specific impairment: it increases by 6 dB for every doubling of the carrier frequency, so the resulting phase-noise distortion must be accounted for explicitly [18, Sec. I-A].

4.1.2 OTFS and DFT-s-OTFS with Superimposed Pilots

A further THz-specific backdrop is multipath sparsity: at 300 GHz only about five surviving multipath components remain, versus roughly eight at mmWave, and the LoS-to-NLoS path-gain gap is about 15 dB larger, so the channel is LoS-dominant with NLoS playing only an auxiliary role [16]. OTFS operates in the delay–Doppler domain and is robust to severe Doppler, but its time-domain samples are equivalent to the inverse-DFT output of the delay–Doppler symbols, so it behaves like OFDM with a relatively high PAPR — lower than OFDM but still unsatisfactory for THz PAs [17, Sec. I]. DFT-spread OTFS (DFT-s-OTFS) applies a DFT spreading operation to the input signal, reducing the PAPR by about 3 dB and bringing it to the level of single-carrier transmission while maintaining Doppler robustness [17, Sec. I-A]. The PA efficiency improvement is substantial: the mean PA efficiency of DFT-s-OTFS is improved by 7% for a class-A PA and by approximately 10% for a class-B PA compared with OTFS [21]. Out-of-band (OOB) radiation is also better: the power leakage at both ends of the transmission band in OTFS and DFT-s-OTFS is approximately 10 dB lower than in OFDM and DFT-s-OFDM [21]. Doppler robustness is confirmed by simulation in a 0.3 THz high-mobility channel, where the BER of DFT-s-OTFS is not degraded by the Doppler effect [21]. Sensing accuracy is high: with a single target the range RMSE is below 10^{-3} m above 10 dB SNR (millimeter-level), and with multiple targets (P = 2, 3) below 10^{-2} m, while velocity estimation achieves decimeter-per-second accuracy, approaching 10^{-1} m/s for two to three targets [21]. At 300 km/h, OFDM and DFT-s-OFDM estimation accuracy degrades, whereas OTFS and DFT-s-OTFS are unaffected [17, Sec. VI-D]. A superimposed-pilot (SP) design removes the dedicated pilot grid, reducing pilot overhead and improving spectral efficiency relative to the embedded-pilot scheme; the pilot symbols carry stronger power than the data symbols and act as a flag for channel-parameter estimation [17, Sec. II-A]. Because pilot and data power compete, an optimal power-allocation problem is solved, yielding $\sigma^2_p = 0.0403$ at 15 dB SNR and 0.0633 at 21 dB SNR, with a saddle point at about 10 dB [17, Sec. V]. The corresponding transceiver chain is shown in Fig. 5(a).

4.1.3 SI-DFT-s-OFDM with CP/FGI Frames and Deep-Learning Receivers

The sensing-integrated DFT-spread OFDM (SI-DFT-s-OFDM) waveform provides lower PAPR than OFDM and adapts to the flexible delay spread of the THz channel [22]. Its key design choice is the frame structure. Unlike the CP scheme, which copies samples of each data block, the flexible guard interval (FGI) is generated by fixed reference symbols inserted into the data blocks, so that the last K_GI samples of each block serve as an approximate cyclic prefix and no extra CP operation is needed [18, Sec. III-B]. This flexibility lowers guard-interval overhead: when the delay spread is 5% of the symbol duration, the FGI scheme supports achievable rates 30 Gbps higher than the CP scheme, with a mean achievable rate of 174 Gbps, about 14 Gbps

© 2026 The Author(s). Authors retain copyright in their articles.

more than CP [22]. The waveform reduces PAPR by approximately 3.2 dB and provides a 5 dB gain at the 10^{-3} BER level compared with OFDM; specifically, the PAPR is approximately 2.6 dB and 3.2 dB lower than OFDM at the 1% CCDF for 64 and 1024 subcarriers, respectively. By reducing PAPR, PA back-off can be decreased and transmit power maximized, yielding the reported 5 dB gain at 10^{-3} BER under MMSE equalization [18, Sec. V-B]. Deep-learning receivers further improve robustness: a two-level ComNet achieves a 2 dB gain at 10^{-3} BER over MMSE under Doppler and outperforms MMSE under phase-noise levels of $\sigma^2_\theta = 10^{-4}$, 10^{-3}, and 10^{-2}; a multiple-input-average-output SensingNet achieves range RMSE below 10^{-2} m (millimeter-level) and the best velocity accuracy among the compared DL methods; and a joint ISACNet reduces network complexity while improving range accuracy relative to separate models, maintaining the same BER [18, Sec. IV–V].

Figure 5: DFT-s-OTFS waveform and learning-based receiver for ISAC. (a) DFT-s-OTFS transceiver with superimposed pilots, supporting active sensing and joint passive sensing with data detection; (b) single-task and two-task deep-learning receivers under the FGI and CP schemes; (c) ISAC-based networking and its key enabling techniques, including beam tracking, MAC/PHY design, and environment perception

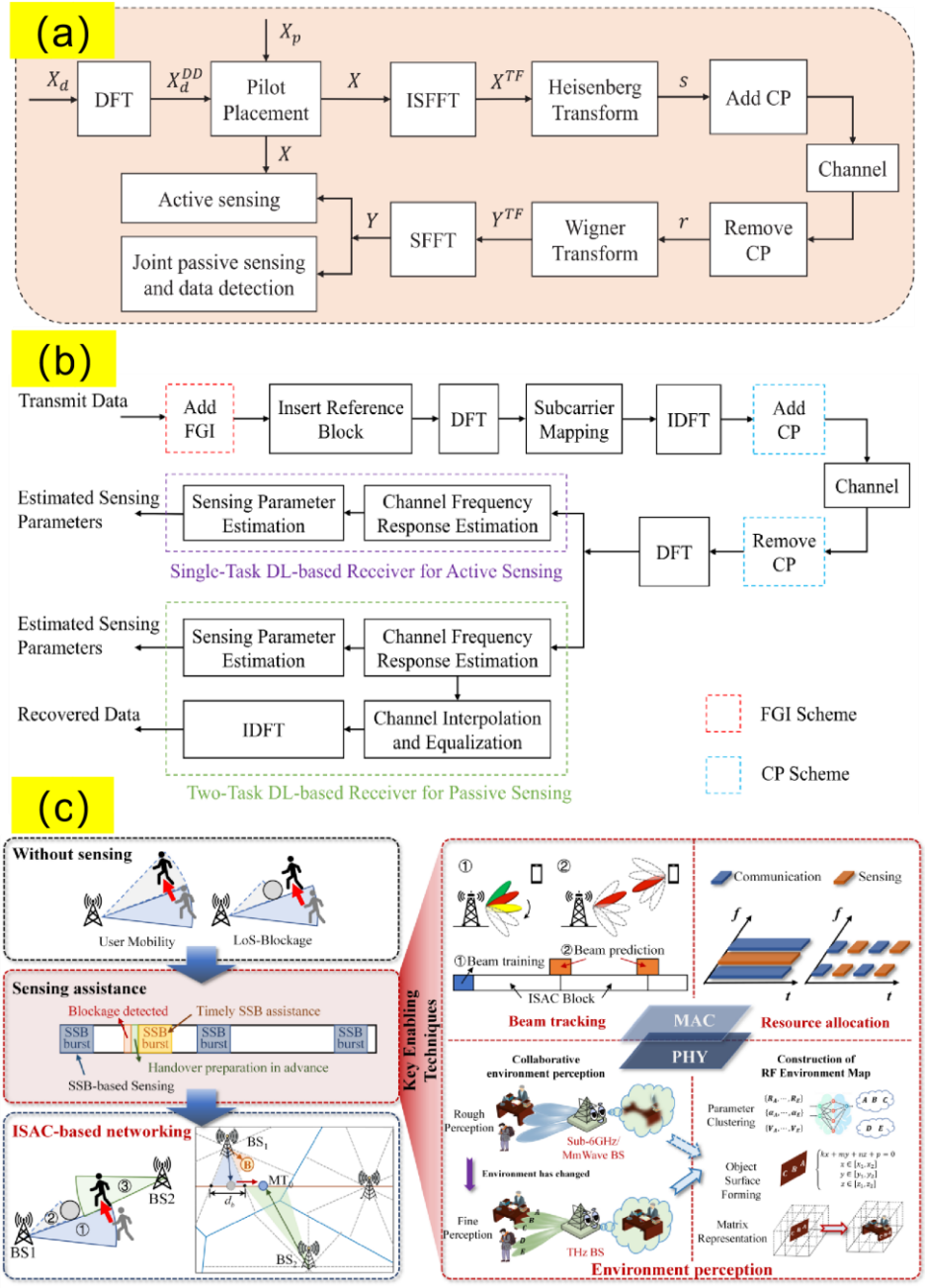

Sources: [14, 21, 22].

© 2026 The Author(s). Authors retain copyright in their articles.

4.1.4 Index Modulation and Joint Waveform Design

Index modulation (IM) encodes additional information in the indices of the transmission media — subcarriers, antennas, and spatial paths — by activating different combinations of RF components, thereby improving spectral efficiency without adding hardware components or interfering with sensing performance [16]. IM-aided ISAC hybrid beamforming exhibits higher spectral efficiency than fully digital beamformers in the evaluated THz-ISAC system [16]. On the UAV side, IM-based ISAC waveforms inherit the low PAPR and superior performance of the original radar-sensing waveform while improving spectral efficiency [4]. IM is therefore a natural bridge between the sensing-centric and communication-centric waveform families in the UAV payload.

4.1.5 Quantified Comparison

Table 1 consolidates the waveform trade-offs, all traced to their original sources.

Table 1: Waveform metrics for THz-ISAC (all values verbatim from the cited sources)

Metric	Value	Reference vs.	Source
DFT-s-OTFS PAPR reduction	≈3 dB	vs. OTFS (continuous-time baseband)	[21], Fig. 5
DFT-s-OTFS PA efficiency	+7% (class A) / +10% (class B), mean	vs. OTFS	[21], Fig. 6
DFT-s-OTFS OOB radiation	≈10 dB lower	OTFS/DFT-s-OTFS vs. OFDM/DFT-s-OFDM	[21], Fig. 7
DFT-s-OTFS BER @0.3 THz, high mobility	not degraded (qualitative)	vs. static channel	[21], Fig. 10
DFT-s-OTFS range RMSE	$<10^{-3}$ m (single target, SNR>10 dB); $<10^{-2}$ m (multi-target)	—	[21], Fig. 11
DFT-s-OTFS velocity RMSE	$\approx 10^{-1}$ m/s (2–3 targets)	—	[21], Fig. 12
Optimal pilot–data power split	σ^2_p = 0.0403 @15 dB; 0.0633 @21 dB; saddle ≈10 dB	—	[21], Fig. 9
SI-DFT-s-OFDM PAPR reduction	2.6 dB (N = 64) / 3.2 dB (N = 1024) @1% CCDF	vs. OFDM	[22], Fig. 6
SI-DFT-s-OFDM BER gain	>5 dB @10^{-3} BER (MMSE)	vs. OFDM	[22], Fig. 7
FGI vs. CP achievable rate	+30 Gbps @5% delay spread; mean 174 Gbps (≈+14 Gbps)	FGI vs. CP	[22], Fig. 8
ComNet BER gain (Doppler)	2 dB @10^{-3} BER	vs. MMSE	[22], Fig. 11
SensingNet range RMSE	$<10^{-2}$ m (millimeter-level)	—	[22], Fig. 9
IM-aided ISAC hybrid BF SE	higher than fully digital	vs. FD beamformers	[16], Fig. 10

4.2 Transceiver Hardware and Implementation

A waveform can only perform as well as the hardware that carries it. We now trace the transceiver chain, payload integration, RF front-end devices, antenna systems, and the digital back-end, against the tight size, weight and power envelope of the UAV. The transceiver chain and its THz-ISAC architecture are summarized in Fig. 6.

The practical superheterodyne front-end implementation of such architectures, comprising the up-/down-conversion, filtering, and amplification stages of the transmit and receive chains, is presented in Fig. 7.

© 2026 The Author(s). Authors retain copyright in their articles.

Figure 6: THz-ISAC system architectures and models. (a) Hybrid analog–digital THz mMIMO-ISAC base station that simultaneously serves communication users and senses multiple targets through shared and echo signals; (b) architectural overview of THz ISAC, including waveform design, algorithm development, RIS-boosted design, and the associated challenges; (c) THz localization system model with an AOSA array and reconfigurable intelligent surfaces; (d) camera-aided ISAC system model for vehicular networks with effective scatterers

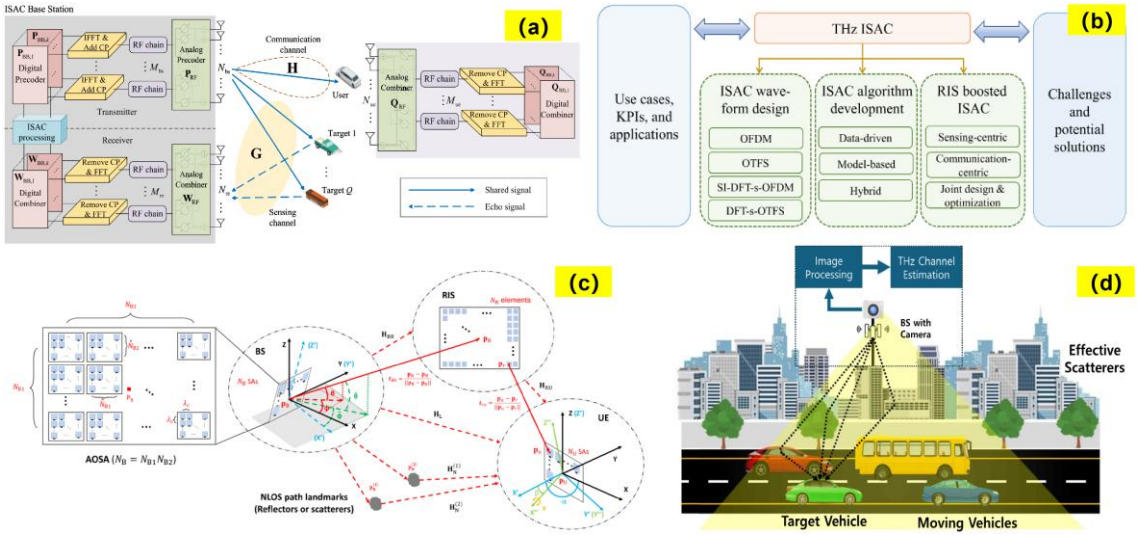

Sources: [4, 15, 41].

Figure 7: Superheterodyne THz transceiver front-ends. (a) Transmitter chain with I/Q up-conversion, IF and THz local oscillators, filtering, and power amplification; (b) receiver chain with low-noise amplification, filtering, and I/Q down-conversion

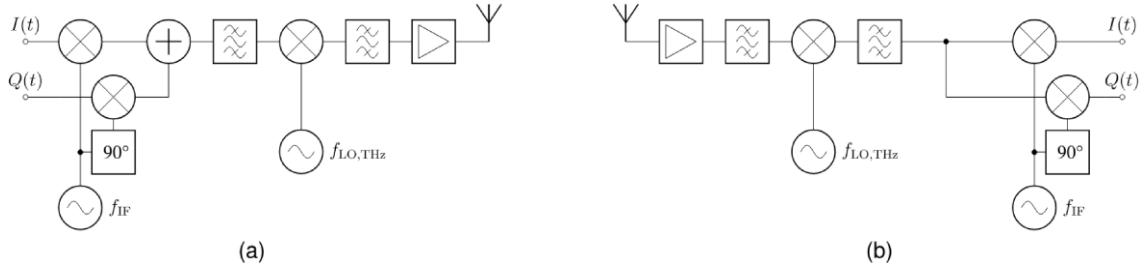

Sources: [15].

4.2.1 UAV Payload Constraints and ISAC Payload Integration

The UAV payload envelope shapes every hardware decision. The stringent power, weight, and size constraints imposed by UAVs, especially for widespread commercial miniaturized drones, make it challenging to accommodate both communication and sensing payloads, and the high power demand of THz-ISAC transceivers causes serious expenditure problems for confined platforms, not to mention the severe round-trip path loss during target sensing [4]. This tension is compounded by the fact that communication and sensing are assessed by different metrics, so a single waveform must satisfy two distinct performance yardsticks at once, and PAPR additionally forces power back-off in the THz front end that further curtails both the communication and sensing ranges [4, 15]. ISAC integration partially mitigates this: shared hardware modules allow the two payloads to be replaced by a single ISAC payload, and the small THz wavelength enables a compact, miniaturized design [4]. The antenna design must provide sufficiently large gain and high directivity to enhance the equivalent isotropic radiated power; programmable metasurfaces with sub-wavelength structures allow a large number of low-cost elements to be integrated for hardware-efficient programmable environments; and sufficient Tx/Rx isolation is necessary to prevent receiver saturation and preserve the dynamic range needed to capture target reflections [4]. On the RF front end, the immaturity of III–V compound-semiconductor transistor technology at THz inherently constrains high-efficiency PAs and high-sensitivity LNAs, restricting the communication and detection distance; because the LNA and PA performance requirements differ between sensing and communication, integrating them into one system must account for these performance differences and for reconfigurable function switching [4].

© 2026 The Author(s). Authors retain copyright in their articles.

4.2.2 RF Front-End: PAs, Multipliers, and Device Technologies

Silicon technologies illustrate the challenge [2]. D-band CMOS PAs achieve a saturated output power P_sat of +18 dBm, a 1-dB gain-compression output power OP1dB of +14 dBm, and a peak power-added efficiency (PAE) of 10–14%, but the modulation energy efficiency is typically below 2%; CMOS circuits approaching 300 GHz deliver transmit power on the order of only 1 mW, suitable only for short-range communication and sensing [8, Sec. III-A]. SiGe devices can achieve f_max over 500 GHz and are less sensitive to layout parasitics, yet similar design trade-offs persist, showing the limitation of silicon-based devices and the need for III–V compound technologies and heterogeneous integration [8, Sec. III-A]. GaN-on-SiC offers much higher performance at W-band, reaching 3 W/mm power density and 45% PAE at 94 GHz, and spatially combining over 8000 GaN-on-SiC MMIC PAs yields a ~6.8 kW W-band transmitter [8, Sec. III-A]. For frequency generation, GaAs-based Schottky diodes serve as multipliers and mixers; frequency-multiplied THz sources provide up to ten times more output power at room temperature than previous state-of-the-art at 180 GHz, 240 GHz, 340 GHz, 530 GHz, 1 THz, and 1.6 THz, and a frequency tripler with 200 mW output power at 225 GHz supports a 2-km multi-Gbps link; the same technology delivers only a few milliwatts at 1 THz [8, Sec. III-A and V].

4.2.3 Antenna Systems: UM Arrays, Metasurfaces, Plasmonic and Leaky-Wave Antennas, Bessel/OAM Beams

To tackle severe THz path loss, extremely dense antenna arrays (e.g., 5 × 5 cm²) composed of thousands of elements are employed; tunable graphene-based plasmonic nanoantennas or metamaterials provide dynamic THz beamforming by steering the main lobe via the graphene layer energy levels, and leaky-wave antennas, whose frequency and beam angle are coupled, are attractive for THz sensing and tracking [16]. Commercially, horn or small dish antennas with gains from 20 to 55 dBi are available, and the small wavelength enables high-gain directional antennas with compact footprints (e.g., 20 dBi in 1 cm²); the far field of a radiating structure scales as $2D^2/\lambda$, so the far field of a 20-cm array begins at 32 m at 120 GHz but not until 280 m at 1.05 THz [8, Sec. III-B and Summary]. Lenses can focus the signal or generate non-diffracting Bessel beams and self-accelerating Airy beams; at 300 GHz (λ = 1 mm) the theoretical footprint of these structures is only 5 cm [6]. OAM beams manifest a spiral phase with a helical wavefront and a central phase singularity, and overlapping helical modes define an orthogonal basis so that different streams can be sent along different OAM modes [6, 42].

4.2.4 Digital Back-End and DSP

The digital back-end limits achievable bandwidth. Data converters with sampling frequencies up to 256 GSaps exist in commercial laboratory-grade equipment; by Nyquist, such converters could operate with analog bandwidths up to f_s/2 (ideally close to 128 GHz), although practically less (e.g., 80 GHz for the cited device); the fastest current SDR platform processes 8 GHz of bandwidth in real time by multiplexing four 2-GHz-wide channels, generating four parallel IQ streams with 1.25 GHz baseband bandwidth each [8, Sec. III–C], [43]. The bandwidth–beamwidth trade-off is fundamental: increasing bandwidth while maintaining SNR (and hence bit rate) requires a major increase in directivity gain and larger radiating structures, which aggravates near-field effects and beam-management complexity [8, Sec. V]. A representative link-budget setting, a 30 m LoS link at 140 GHz, Tx 100 mW with 20 dBi, Rx noise figure 20 dB and antenna gain 0–40 dBi, shows the minimum antenna gain needed to achieve SNR of at least 10, 15, and 20 dB [6]. Reported sensing ranges include pedestrian detection up to 20 m and car detection up to 50 m for a 290 GHz automotive radar, and a Tx gain of 26 dBi with 3.6° beamwidth at about 10 m [16].

5. System-Level Performance and Applications

5.1 Localization and Performance Bounds

THz localization exploits four basic geometric measurements — TOA, TDOA, AOA, and AOD — and their combinations, with the number of base stations and measurements required per metric summarized in the tutorial [41]. The channel model incorporates molecular absorption via the HITRAN database, and the antenna gain is described by an ideal sector model or a Gaussian beam model [41]. Performance bounds (PEB/OEB/CRB) quantify the potential: moving the carrier from 60 GHz to 300 GHz increases the error bound

© 2026 The Author(s). Authors retain copyright in their articles.

because of high path loss, but increasing the antenna spacing from 0.5λ to 2.5λ and adopting an AOSA structure with a 5 × 5 sub-array introduces beamforming gain that outperforms the mmWave benchmark. The bounds also improve with larger bandwidth (1 GHz versus 100 MHz) and with prior information [41]. Overall, approximately 5× (without prior information) and 20× (with prior information) better positioning performance is expected at THz than at mmWave for the same power and footprint, although multiple transmissions and prior knowledge are required to resolve the deafness issue [41]. Beam split, normally harmful to communications, can provide extra geometric information because beams at different subcarriers point in different directions, lowering the error bound in wideband systems [41]; RIS dimensions, quantization, and NLoS coefficients further modulate the CRB [41]. The resulting localization performance bounds are shown in Fig. 8, together with the waveform-level PAPR and achievable-rate trends discussed in Section 4.1.

Figure 8: Waveform and localization performance of THz-ISAC. (a) PAPR CCDF for OFDM, DFT-s-OFDM, OTFS, and DFT-s-OTFS with different pilot powers; (b) achievable rate versus delay spread for the CP and FGI frame structures; (c) RMSE versus transmit power for the proposed algorithm, the tensor-based and MUSIC baselines, and the CRB; (d) PEB and (e) OEB versus the number of antennas/sensing elements; (f) antenna-array configurations for the mmWave and THz systems

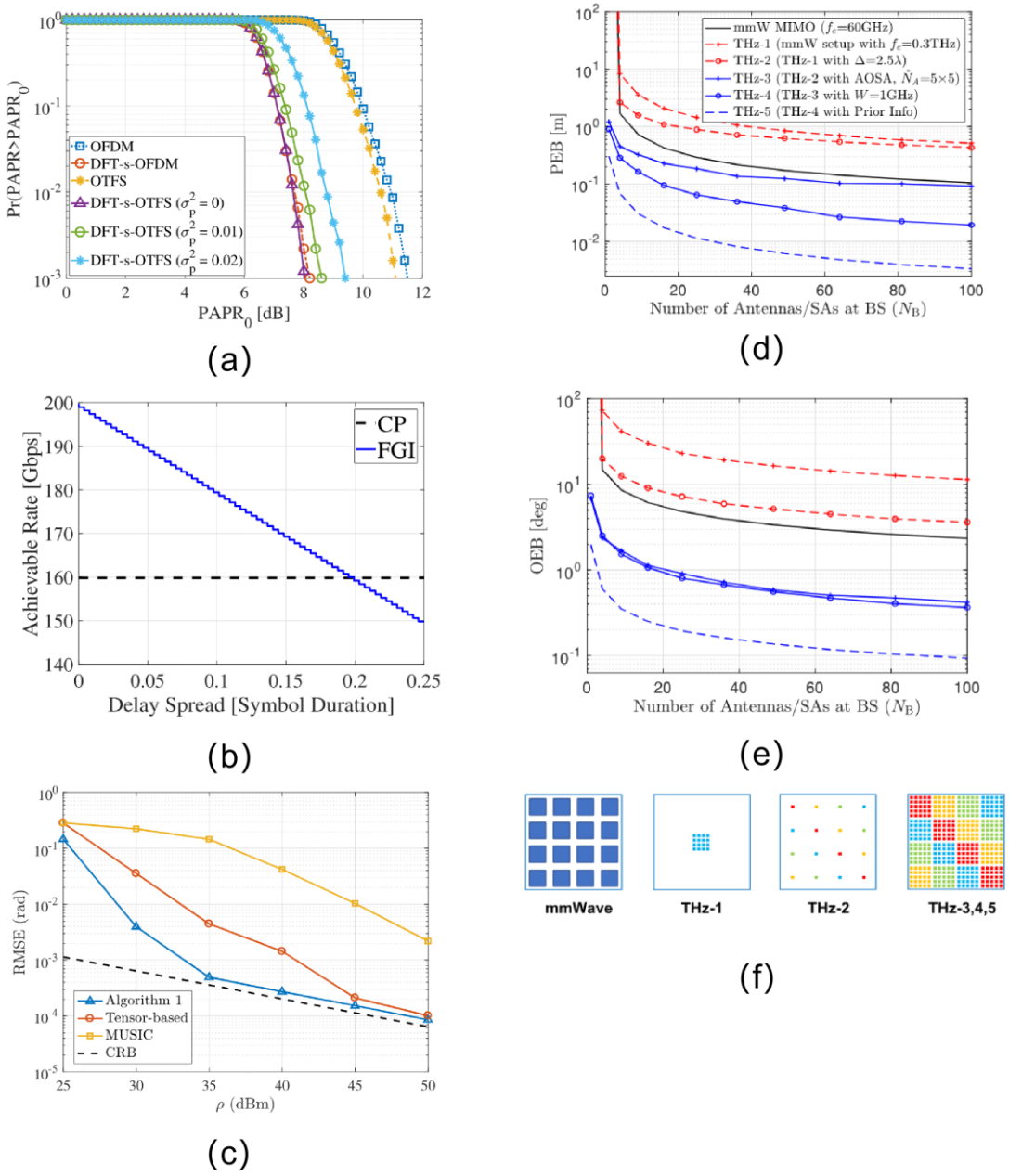

Sources: [21, 22, 41].

© 2026 The Author(s). Authors retain copyright in their articles.

5.2 Spectral Efficiency and Throughput

The waveform and beam architectures in Sections 3.3 and 4.1 are evaluated in terms of spectral efficiency (SE) and energy efficiency (EE). Compared with the optimal precoding and the FC-TTD architecture, the DS-FTTD architecture with the RD algorithm is about 4 and 3 bit/s/Hz lower in SE, respectively, while it exceeds FC-PS and DS-PS by about 2 and 3 bit/s/Hz at ρ = 20 dBm, and AoSA/GoSA are 8 and 8.3 bit/s/Hz lower, revealing a favorable SE–EE trade-off [38]. Reported sensing/vision-aided mobility management achieves more than 30% throughput gain over conventional techniques [44, 45]. Viewed together, these results point toward the broader vision of a 'network-as-a-sensor' in which sensing and communication reinforce each other, rather than compete for the same resources [15].

In ultra-dense mmWave/THz networks, a reliable path can disappear after even a small movement of a mobile, making cell association challenging [40]. A sensing- and computer-vision (CV)-based mobility-management technique predicts the cell association from visual sensing information: geometric information of the mobile is extracted from the image and used for downlink-rate prediction, enabling preemptive cell-association switching in the UDN; numerical evaluation on realistic mmWave/THz UDN environments shows more than 30% throughput gain [44]. In the simulations, ray tracing identifies LoS paths and a 3GPP TR 38.901 path-loss model generates the channel, with obstacle densities of ρ_o = 10%, 20%, and 30%, and a localization error $p_{err} \sim N(3.64\ \text{cm}, 7.56\ \text{cm}^2)$ added to the ground-truth position before input to the TORP network [44]. Real-time learning from THz radar mapping has been used to close the sense–act loop for UAV control [46].

Data-driven methods now address channel estimation: vision-and-causal-learning-based channel estimation exploits a visual causal-discovery (VCD) causal graph relating channel variables to environmental features, and studies counterfactual cross-scenario generalization and domain-guided methods; performance degrades as the number of paths increases, and the importance of channel parameters varies over time. Beyond channel estimation, deep reinforcement learning has been applied to joint resource allocation and trajectory planning in ISAC UAV networks, co-optimizing communication and sensing utilities [47]. However, data-driven methods are not yet well tailored to the payload design, which demands low computational delay, storage, and complexity [48]; the high-speed UAV movement and ultra-narrow UM-MIMO beams pose significant challenges for training-set size and transfer-learning capability [4].

5.3 Use Cases and Applications

THz use cases can be classified by mobility, from inherently stationary systems such as wireless networks-on-chip, board-to-board links, data-center links, and fronthaul/backhaul, through low- and medium-speed systems such as nanosensor networks, imaging, kiosk download, femto/micro cells, automotive radars, and vehicular communications, to highly mobile systems such as airborne-node connectivity, satellite remote sensing, and LEO satellite communication [6]. Applications span from space to ground and from macro-scale to nano-scale [13, 49]: satellite-to-ground, satellite-to-aircraft, and inter-satellite links [12, 27]; indoor office, wireless data center and backhaul, kiosk, multimedia, and short-range desktop links; and on-chip/inter-chip communication and wireless nanosensor networks [5]. For UAVs in particular, THz-ISAC unifies both functionalities in a single system, opening new opportunities for ultra-high-rate communication and sensing [4, 45, 50, 51]. Representative enablers include a 3D multi-UAV radio-access network with THz-empowered backhaul that interconnects aerial cells [52], joint THz sensing-and-communication optimization for vehicular networks based on dynamic graph neural networks [53], a THz-band UAV base station for post-disaster communication that restores coverage where terrestrial infrastructure is damaged [54], UAV-relay-enabled THz covert communication against colluding detection [55], and THz-based precision agriculture supporting plant-level monitoring [56].

6. Open Challenges and Conclusion

6.1 Open Challenges and Future Directions

(1) A unified ground-to-UAV channel model. Measured data remain concentrated in indoor and urban terrestrial scenarios [5, 9, 10, 11], while dedicated air-ground statistical models are scarce and are currently approached mainly through terrestrial GBSMs extended with altitude-dependent absorption and 3D UAV

© 2026 The Author(s). Authors retain copyright in their articles.

geometry [8, 17, 18]. A unified model spanning the ground and air domains, necessary for cross-layer co-design of integrated ground-to-UAV networks, remains open; closing it will require measurement campaigns across a much wider set of aerial, vehicular, maritime, and satellite scenarios than are available today [3, 16].

(2) Measurement scarcity above 300 GHz and real-time tracking. Measured data above 300 GHz are still scarce, and real-time channel tracking and prediction under high dynamics are at an early stage, struggling to satisfy the simultaneous demand for timeliness and accuracy [6, 9, 19].

(3) Joint communication–sensing optimization, metrics, and standardization. Existing fundamental-limit studies focus on achievable rate, estimation accuracy, and transmit beam pattern, but generally overlook energy-efficiency-related metrics. From a sensing perspective, moreover, the concept of information freshness has not been defined as clearly as for communications, and how age-of-information (AoI) can guarantee timely information delivery and acquisition requires further investigation in THz-ISAC-UAV systems [4, 50, 51]. A joint communication–sensing channel-characterization framework, together with the standardization of its metrics, is also still missing [4, 16].

(4) Hardware non-idealities and low-power implementation. THz RF front-end impairments, such as local-oscillator phase noise and PA nonlinear distortion, fundamentally limit performance; synchronization errors (frequency offset and timing error) are exacerbated by UAV mobility, especially degrading sensing accuracy [4]. The immature III–V technology and the UAV power budget further constrain PA/LNA performance [4, 6, 42, 43].

(5) Lightweight machine learning and domain generalization. Deep-learning methods are not yet tailored to the UAV payload's low-latency, low-storage, low-complexity requirements, and the combination of high-speed movement and ultra-narrow beams challenges training-set size and transfer learning [4]; near-field and beam-split effects further weaken domain generalization [34, 41, 48, 57].

6.2 Conclusion

This survey has reviewed THz-ISAC for ground-to-UAV channels along four coupled pillars. For channel modeling, the field is converging from ad hoc large-scale fits toward statistical and geometry-based models: measured path-loss exponents fall below the FSPL value (≈1.77–1.84) because of reflections and waveguiding, delay and angular spreads follow log-normal statistics while the K-factor is normal, and a first three-dimensional GBSM now captures UAV movement and antenna orientation, yet altitude-dependent absorption, wind-driven non-stationarity, and near-field/beam-split behavior still lack dedicated air-ground models [17, 18]. For beam management, the trajectory is toward ISAC-assisted, predictive alignment (≈70% misalignment reduction, with corresponding average coverage gains on the order of 36%) and toward wideband hybrid architectures (DS-FTTD) that trade a small spectral-efficiency loss for large energy-efficiency gains while resolving 22 dB-scale beam-squint loss [38]. For waveforms, the design axis is low PAPR plus Doppler robustness: DFT-s-OTFS delivers ≈3 dB PAPR reduction, +7–10% PA efficiency, and ≈10 dB lower OOB radiation with millimeter-level ranging and decimeter-per-second velocimetry [21], while SI-DFT-s-OFDM with flexible guard intervals reduces PAPR by up to 3.2 dB and raises the achievable rate by tens of Gbps [22]. Transceiver hardware, constrained by the UAV payload and by silicon/III–V maturity, remains the practical bottleneck. The next stage of the field will be defined by the unification of the ground and air channel models and by system-level co-design of waveform, beam, and hardware under a shared energy budget.

References

[1] D. Serghiou, M. Khalily, T. W. C. Brown, and R. Tafazolli, “Terahertz Channel Propagation Phenomena, Measurement Techniques and Modeling for 6G Wireless Communication Applications: A Survey, Open Challenges and Future Research Directions,” *IEEE Commun. Surv. Tutorials*, vol. 24, no. 4, pp. 1957–1996, 2022, doi: 10.1109/COMST.2022.3205505.

[2] T. S. Rappaport *et al.*, “Wireless Communications and Applications Above 100 GHz: Opportunities and Challenges for 6G and Beyond,” *IEEE Access*, vol. 7, pp. 78729–78757, 2019, doi: 10.1109/ACCESS.2019.2921522.

© 2026 The Author(s). Authors retain copyright in their articles.

[3] C. Han *et al.*, "Terahertz Wireless Channels: A Holistic Survey on Measurement, Modeling, and Analysis," *IEEE Commun. Surv. Tutorials*, vol. 24, no. 3, pp. 1670–1707, 2022, doi: 10.1109/COMST.2022.3182539.

[4] R. Zhang, W. Wu, X. Chen, Z. Gao, and Y. Cai, "Terahertz Integrated Sensing and Communication-Empowered UAVS in 6G: A Transceiver Design Perspective," *IEEE Veh. Technol. Mag.*, vol. 21, no. 1, pp. 71–80, Mar. 2026, doi: 10.1109/MVT.2025.3531088.

[5] J. Wang, C.-X. Wang, J. Huang, and Y. Chen, "6G THz Propagation Channel Characteristics and Modeling: Recent Developments and Future Challenges," *IEEE Commun. Mag.*, vol. 62, no. 2, pp. 56–62, Feb. 2024, doi: 10.1109/MCOM.001.2200403.

[6] J. M. Jornet *et al.*, "The Evolution of Applications, Hardware Design, and Channel Modeling for Terahertz (THz) Band Communications and Sensing: Ready for 6G?," *Proc. IEEE*, vol. 113, no. 9, pp. 920–951, Sep. 2025, doi: 10.1109/JPROC.2024.3412828.

[7] J. M. Jornet and I. F. Akyildiz, "Channel Modeling and Capacity Analysis for Electromagnetic Wireless Nanonetworks in the Terahertz Band," *IEEE Transactions on Wireless Communications*, vol. 10, no. 10, pp. 3211–3221, 2011, doi: 10.1109/TWC.2011.081011.100545.

[8] D. Li *et al.*, "Ground-to-UAV sub-terahertz channel measurement and modeling," *Opt. Express*, vol. 32, no. 18, p. 32482, Aug. 2024, doi: 10.1364/OE.534369.

[9] Z. Chang *et al.*, "3GPP-Like GBSM THz Channel Characterization, Modeling, and Simulation Based on Experimental Observations," *Tsinghua Science and Technology*, vol. 31, no. 3, pp. 1556–1577, 2026, doi: 10.26599/tst.2024.9010237.

[10] Y. Lyu, Z. Yuan, P. Zhang, Z. Huang, P. Kyösti, and W. Fan, "Large Virtual Antenna Array-Based Empirical Channel Characterization for Sub-THz Indoor Hall Scenarios," *IEEE Trans. Antennas Propagat.*, vol. 73, no. 4, pp. 2000–2011, Apr. 2025, doi: 10.1109/TAP.2024.3423470.

[11] N. A. Abbasi *et al.*, "THz Band Channel Measurements and Statistical Modeling for Urban D2D Environments," *IEEE Transactions on Wireless Communications*, vol. 22, no. 3, pp. 1466–1479, 2023, doi: 10.1109/TWC.2022.3184929.

[12] S. A. Torrens, V. Petrov, and J. M. Jornet, "Modeling Interference From Millimeter Wave and Terahertz Bands Cross-Links in Low Earth Orbit Satellite Networks for 6G and Beyond," *IEEE J. Select. Areas Commun.*, vol. 42, no. 5, pp. 1371–1386, May 2024, doi: 10.1109/JSAC.2024.3365894.

[13] X. Yuan, F. Tang, M. Zhao, and N. Kato, "Joint Rate and Coverage Optimization for the THz/RF Multi-Band Communications of Space-Air-Ground Integrated Network in 6G," *IEEE Trans. Wireless Commun.*, vol. 23, no. 6, pp. 6669–6682, Jun. 2024, doi: 10.1109/TWC.2023.3336016.

[14] L. Li, W. Chen, Z. Chen, T. Hu, W. Mei, and B. Ning, "Enhancing Terahertz Communications Coverage with ISAC-Assisted Beam Management," *IEEE Wireless Commun.*, vol. 31, no. 1, pp. 34–40, Feb. 2024, doi: 10.1109/MWC.002.2300291.

[15] W. Jiang *et al.*, "Terahertz Communications and Sensing for 6G and Beyond: A Comprehensive Review," *IEEE Commun. Surv. Tutorials*, vol. 26, no. 4, pp. 2326–2381, 2024, doi: 10.1109/COMST.2024.3385908.

[16] A. M. Elbir, K. V. Mishra, S. Chatzinotas, and M. Bennis, "Terahertz-Band Integrated Sensing and Communications: Challenges and Opportunities," *IEEE Aerosp. Electron. Syst. Mag.*, vol. 39, no. 12, pp. 38–49, Dec. 2024, doi: 10.1109/MAES.2024.3476228.

[17] Z. Jiang, Y. Li, K. Zhang, and J. Liu, "A Non-Stationary Geometry-Based MIMO Channel Model for Terahertz UAV-Based Wireless Communication Systems," *ENTROPY*, vol. 28, no. 7, Jul. 2026, doi: 10.3390/e28070744.

[18] H. Wang, D. Sun, C. Sun, and C. Zhu, "A Physical Air-to-Ground Modeling Method with Dynamic Investigations for Integrated Sensing and Communication," *JOURNAL OF COMMUNICATIONS AND NETWORKS*, vol. 26, no. 5, pp. 509–520, Oct. 2024, doi: 10.23919/JCN.2024.000041.

© 2026 The Author(s). Authors retain copyright in their articles.

[19] Y. Chen, C. Han, Z. Yu, and G. Wang, "Channel Measurement, Characterization, and Modeling for Terahertz Indoor Communications Above 200 GHz," *IEEE TRANSACTIONS ON WIRELESS COMMUNICATIONS*, vol. 23, no. 6, pp. 6518–6532, Jun. 2024, doi: 10.1109/TWC.2023.3333222.

[20] X. Wang, C. Huang, G. Gou, L. Liang, H. Zeng, and Y. Zhang, "Dynamic Beam Management for High–Low-Frequency UAV Networks," *IEEE Internet Things J.*, vol. 13, no. 9, pp. 19250–19260, May 2026, doi: 10.1109/JIOT.2026.3662785.

[21] Y. Wu, C. Han, and Z. Chen, "DFT-Spread Orthogonal Time Frequency Space System With Superimposed Pilots for Terahertz Integrated Sensing and Communication," *IEEE Trans. Wireless Commun.*, vol. 22, no. 11, pp. 7361–7376, Nov. 2023, doi: 10.1109/TWC.2023.3250267.

[22] Y. Wu, F. Lemic, C. Han, and Z. Chen, "Sensing Integrated DFT-Spread OFDM Waveform and Deep Learning-Powered Receiver Design for Terahertz Integrated Sensing and Communication Systems," *IEEE Trans. Commun.*, vol. 71, no. 1, pp. 595–610, Jan. 2023, doi: 10.1109/TCOMM.2022.3225920.

[23] Y. Zhang, Q. Li, J. Wang, J. Wang, J. Chen, and Z. Han, "Toward Throughput Maximization of Integrated Sensing and Communications Enabled Predictive Beamforming for 6G," *IEEE NETWORK*, vol. 38, no. 4, pp. 292–300, Jul. 2024, doi: 10.1109/MNET.2023.3326067.

[24] T. Mao, J. Chen, Q. Wang, C. Han, Z. Wang, and G. Karagiannidis, "Waveform Design for Joint Sensing and Communications in Millimeter-Wave and Low Terahertz Bands," *IEEE TRANSACTIONS ON COMMUNICATIONS*, vol. 70, no. 10, pp. 7023–7039, Oct. 2022, doi: 10.1109/TCOMM.2022.3196685.

[25] IEEE, *IEEE Standard for High Data Rate Wireless Multi-Media Networks—Amendment 2: 100 Gb/s Wireless Switched Point-to-Point Physical Layer*, 802.15.3d-2017, 2017. doi: 10.1109/IEEESTD.2017.8066476.

[26] T. Kürner, A. F. Molisch, and M. Shafi, "Review of Wireless Propagation Research—Past, Current and Future Developments," *IEEE Trans. Antennas Propagat.*, vol. 74, no. 5, pp. 3847–3864, May 2026, doi: 10.1109/TAP.2026.3675326.

[27] W. Gao, C. Han, Y. Chen, Y. He, and W. Zhang, "Terahertz aerospace communications: enabling technologies and future directions," *SCIENCE CHINA-INFORMATION SCIENCES*, vol. 68, no. 12, Nov. 2025, doi: 10.1007/s11432-025-4652-0.

[28] Y. Chen, R. Li, C. Han, S. Sun, and M. Tao, "Hybrid Spherical- and Planar-Wave Channel Modeling and Estimation for Terahertz Integrated UM-MIMO and IRS Systems," *IEEE Trans. Wireless Commun.*, vol. 22, no. 12, pp. 9746–9761, Dec. 2023, doi: 10.1109/TWC.2023.3273221.

[29] W. Xia, V. Semkin, M. Mezzavilla, G. Loianno, and S. Rangan, "Multi-Array Designs for mmWave and Sub-THz Communication to UAVs," in *2020 IEEE 21st International Workshop on Signal Processing Advances in Wireless Communications (SPAWC)*, 2020, pp. 1–5. doi: 10.1109/spawc48557.2020.9153882.

[30] P. Zhang *et al.*, "Evaluating the Beamforming Impact on Channel Dispersion Characterization Using Multiscenario Sub-THz Channel Measurements," *IEEE TRANSACTIONS ON ANTENNAS AND PROPAGATION*, vol. 73, no. 1, pp. 469–481, Jan. 2025, doi: 10.1109/TAP.2024.3489959.

[31] J. Wang, C.-X. Wang, J. Huang, H. Wang, and X. Gao, "A General 3D Space-Time-Frequency Non-Stationary THz Channel Model for 6G Ultra-Massive MIMO Wireless Communication Systems," *IEEE Journal on Selected Areas in Communications*, vol. 39, no. 6, pp. 1576–1589, 2021, doi: 10.1109/JSAC.2021.3071850.

[32] Q. Xue *et al.*, "A Survey of Beam Management for mmWave and THz Communications Towards 6G," *IEEE COMMUNICATIONS SURVEYS AND TUTORIALS*, vol. 26, no. 3, pp. 1520–1559, Apr. 2024, doi: 10.1109/COMST.2024.3361991.

[33] B. Chang, Z. Chen, W. Tang, L. Li, H. Zhang, and X. Liao, "Joint Sensing, Control, and Communication Scheduling for THz Beam Alignment in Cellular Connected UAV Networks," in *2021 IEEE International Symposium on Dynamic Spectrum Access Networks (DySPAN)*, 2021, pp. 61–66. doi: 10.1109/DySPAN53946.2021.9677081.

© 2026 The Author(s). Authors retain copyright in their articles.

[34] S. K. Moorthy and Z. Guan, “Beam Learning in MmWave/THz-Band Drone Networks Under In-Flight Mobility Uncertainties,” *IEEE Transactions on Mobile Computing*, vol. 21, no. 6, pp. 1945–1957, 2022, doi: 10.1109/TMC.2020.3034064.

[35] Z.-J. Wang, A. Tang, and X. Wang, “Theoretical Performance Study for mmWave/THz ISAC Systems With Sensing-Based Beam Alignment,” *IEEE Transactions on Vehicular Technology*, vol. 75, no. 8, pp. 17562–17575, 2026, doi: 10.1109/TVT.2026.3679354.

[36] Z. Yang, S. Gao, X. Cheng, and L. Yang, “Synesthesia of Machines (SoM)-Enhanced Sub-THz ISAC Transmission for AirGround Network,” *IEEE TRANSACTIONS ON WIRELESS COMMUNICATIONS*, vol. 25, pp. 9295–9312, 2026, doi: 10.1109/TWC.2025.3649505.

[37] A. M. Elbir, A. Abdallah, A. Celik, and A. M. Eltawil, “Antenna Selection With Beam Squint Compensation for Integrated Sensing and Communications,” *IEEE J. Sel. Top. Signal Process.*, vol. 18, no. 5, pp. 857–870, Jul. 2024, doi: 10.1109/JSTSP.2024.3378909.

[38] L. Yan, C. Han, and J. Yuan, “Energy-Efficient Dynamic-Subarray With Fixed True-Time-Delay Design for Terahertz Wideband Hybrid Beamforming,” *IEEE J. Select. Areas Commun.*, vol. 40, no. 10, pp. 2840–2854, Oct. 2022, doi: 10.1109/JSAC.2022.3196090.

[39] R. Zhang *et al.*, “Channel-Training-Aided Target Sensing for Terahertz Integrated Sensing and Massive MIMO Communications,” *IEEE Internet Things J.*, vol. 12, no. 4, pp. 3755–3770, Feb. 2025, doi: 10.1109/JIOT.2024.3447584.

[40] B. Chang, W. Tang, X. Yan, X. Tong, and Z. Chen, “Integrated Scheduling of Sensing, Communication, and Control for mmWave/THz Communications in Cellular Connected UAV Networks,” *IEEE JOURNAL ON SELECTED AREAS IN COMMUNICATIONS*, vol. 40, no. 7, pp. 2103–2113, Jul. 2022, doi: 10.1109/JSAC.2022.3157366.

[41] H. Chen, H. Sarieddeen, T. Ballal, H. Wymeersch, M.-S. Alouini, and T. Y. Al-Naffouri, “A Tutorial on Terahertz-Band Localization for 6G Communication Systems,” *IEEE Commun. Surv. Tutorials*, vol. 24, no. 3, pp. 1780–1815, 2022, doi: 10.1109/COMST.2022.3178209.

[42] R. Singh, I. Ahmad, F. Alanazi, and D. Alqahtani, “Next-Generation Reconfigurable Antenna Systems for 6G: Challenges, Architectures, and Vision,” *IEEE Access*, vol. 13, pp. 196355–196373, 2025, doi: 10.1109/ACCESS.2025.3633193.

[43] S. Sivasankar *et al.*, “Joint Communication and Sensing at D-Band SDR and at 5.8 GHz via Multibeam Arrays,” *IEEE TRANSACTIONS ON MICROWAVE THEORY AND TECHNIQUES*, vol. 73, no. 6, pp. 3236–3249, Jun. 2025, doi: 10.1109/TMTT.2025.3566499.

[44] Y. Ahn, J. Kim, S. Kim, S. Kim, and B. Shim, “Sensing and Computer Vision-Aided Mobility Management for 6G Millimeter and Terahertz Communication Systems,” *IEEE Trans. Commun.*, vol. 72, no. 10, pp. 6044–6058, Oct. 2024, doi: 10.1109/TCOMM.2024.3392799.

[45] Y. Gao, H. Xue, L. Zhang, and E. Sun, “UAV Trajectory Design and Power Optimization for Terahertz Band-Integrated Sensing and Communications,” *SENSORS*, vol. 23, no. 6, Mar. 2023, doi: 10.3390/s23063005.

[46] A. Guerra, F. Guidi, D. Dardari, and P. M. Djuric, “Real-Time Learning for THZ Radar Mapping and UAV Control,” *2021 IEEE International Conference on Autonomous Systems (ICAS)*, pp. 1–5, 2021, doi: 10.1109/ICAS49788.2021.9551141.

[47] Y. Qin, Z. Zhang, X. Li, W. Huangfu, and H. Zhang, “Deep Reinforcement Learning Based Resource Allocation and Trajectory Planning in Integrated Sensing and Communications UAV Network,” *IEEE Transactions on Wireless Communications*, vol. 22, no. 11, pp. 8158–8169, 2023, doi: 10.1109/TWC.2023.3260304.

[48] G. Fontanesi *et al.*, “A Deep-NN Beamforming Approach for Dual Function Radar-Communication THz UAV,” *IEEE TRANSACTIONS ON VEHICULAR TECHNOLOGY*, vol. 74, no. 1, pp. 746–760, Jan. 2025, doi: 10.1109/TVT.2024.3453194.

© 2026 The Author(s). Authors retain copyright in their articles.

[49] J. Liu, X. Yang, Y. Wei, and F. Zhao, "Integrated THz/FSO Communications: A Review of Practical Constraints, Applications and Challenges," *Micromachines*, vol. 16, no. 11, p. 1297, Nov. 2025, doi: 10.3390/mi16111297.

[50] Y. Liu *et al.*, "Radar Probing Optimization for Joint Beamforming and UAV Trajectory Design in UAV-Enabled Integrated Sensing and Communication," *IEEE TRANSACTIONS ON COMMUNICATIONS*, vol. 73, no. 6, pp. 4469–4485, Jun. 2025, doi: 10.1109/TCOMM.2024.3506917.

[51] W. Wang, X. Liu, and Z. Liu, "Joint Beamforming and Trajectory Design for Multi-Antenna UAV-Enabled ISAC," *IEEE TRANSACTIONS ON VEHICULAR TECHNOLOGY*, vol. 75, no. 2, pp. 3283–3287, Feb. 2026, doi: 10.1109/TVT.2025.3600883.

[52] K. Kim and J. P. Choi, "3D Network Design for Multi-UAV RAN With THz-Empowered Backhaul," *IEEE Transactions on Wireless Communications*, vol. 23, no. 11, pp. 16437–16452, 2024, doi: 10.1109/twc.2024.3440923.

[53] X. Li, M. Chen, Y. Hu, Z. Zhang, D. Liu, and S. Mao, "Jointly Optimizing Terahertz Based Sensing and Communications in Vehicular Networks: A Dynamic Graph Neural Network Approach," *IEEE Transactions on Wireless Communications*, vol. 23, no. 10, pp. 12917–12932, 2024, doi: 10.1109/twc.2024.3397028.

[54] S. Barhoumi, M. Erdem, and M.-S. Alouini, "Terahertz Band UAV Base Stations for Post-Disaster Communication," *IEEE Open Journal of the Communications Society*, vol. 6, pp. 4788–4803, 2025, doi: 10.1109/ojcoms.2025.3574264.

[55] X. Pi, B. Yang, Y. Shen, and X. Jiang, "UAV Relay-Enabled THz Covert Communications Against Colluding Detection," *Transactions on Emerging Telecommunications Technologies*, vol. 36, no. 6, 2025, doi: 10.1002/ett.70165.

[56] M. Usman, S. Ansari, A. Taha, A. Zahid, Q. H. Abbasi, and M. A. Imran, "Terahertz-Based Joint Communication and Sensing for Precision Agriculture: A 6G Use-Case," *Frontiers in Communications and Networks*, vol. 3, 2022, doi: 10.3389/frcmn.2022.836506.

[57] K. Kim, Y. K. Tun, Md. S. Munir, C. K. Thomas, W. Saad, and C. S. Hong, "Vision and Causal Learning Based Channel Estimation for THz Communications," *IEEE Trans. on Mobile Comput.*, vol. 25, no. 8, pp. 12385–12403, Aug. 2026, doi: 10.1109/TMC.2026.3673506.

Funding

This research received no external funding.

Conflicts of Interest

The authors declare no conflict of interest.

Acknowledgment

This paper is an output of the science project.

Copyrights

Copyright for this article is retained by the author (s), with first publication rights granted to the journal. This is an open-access article distributed under the terms and conditions of the Creative Commons Attribution license (http://creativecommons.org/licenses/by/4.0/).

© 2026 The Author(s). Authors retain copyright in their articles.